

Large-Signal Response of p-i-n Photodetectors Using Short Pulses With Small Spot Sizes

Micah B. Yairi, Hilmi Volkan Demir, Petar B. Atanackovic, *Member, IEEE*, and David A. B. Miller, *Fellow, IEEE*

Abstract—In this paper, the response of a surface-normal p-i-n photodetector that was incorporated in an optically controlled optical gate was analyzed using short-pulsed, high-energy optical inputs with small spot sizes. Simulation results based in part on diffusive conduction were compared against the experimental data, providing an understanding of the device response. Results also demonstrated that p-i-n photodetectors may be designed so that reducing the spot size, counterintuitively, results in negligible additional field screening.

Index Terms—Diffusive conduction, large-signal, optoelectronic, photodetector, short-pulse.

I. INTRODUCTION

P-I-N photodetectors are ubiquitous in optoelectronic circuits. They are used in countless applications such as high speed receivers, optical modulators, and solar energy collectors. Yet another application of p-i-n photodetectors is their use in optically controlled optical gates (OCOGs) that can be utilized for ultrafast optoelectronic optical switching, time division demultiplexing, or wavelength conversion in wavelength-division-multiplexed (WDM) transmission systems. [1], [2] Often it is critical to understand the response of p-i-n detectors to large-signal optical inputs. For example, large-optical signal response behavior is important in analog devices such as analog-to-digital converters, where linear photodetector response is often essential for accurate device operation. Nonlinear responses (e.g., due to saturation) may restrict the optical intensity level that may be used. Several papers have reported the details of photodetector large-signal behavior in general, their modeling, or both. [3]–[12] Photodetector large-signal response depends on how the voltage change due to photogenerated charge separation rises and relaxes. There are two primary voltage relaxation processes: a global effect, voltage decay through the external circuitry, and a local effect, voltage diffusion—also referred to as diffusive conduction. There has been, however, relatively little investigation of the local voltage relaxation process and its effect on the spatio-temporal response to large-signal input optical pulses, even though photodetector response is known to be a sensitive function of both spot size and input power. For such a study of the photodetector internal dynamics, measuring the output current alone does not provide detailed information; the local voltage (or current) response must be investigated.

In this paper we report what we believe is the first experimental testing and modeling of a subclass of p-i-n photodetec-

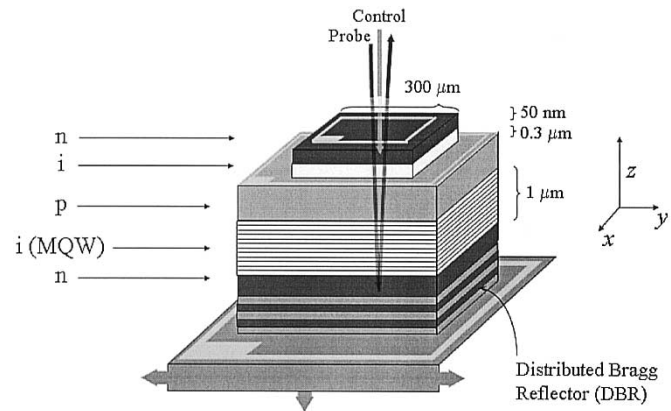


Fig. 1. Diagram of a dual-diode optically controlled optical gate. The $\text{Al}_{0.08}\text{Ga}_{0.92}\text{As}$ n-i-p-i (MQW)-n device was grown on top of a DBR mirror stack centered at 855 nm. There were 69 95-Å GaAs wells with 50-Å AlAs barriers in the MQW region. An antireflection Si_3N_4 layer was sputtered on top.

tors: those that use normally incident short pulses of light with small spot sizes, providing the potential to study their spatio-temporal response. The response in this type of photodetector is, by design, strongly dependent on the local voltage decay behavior. Small-signal modeling of such detectors has been reported by several groups. [13]–[17] To the best of our knowledge, though, their large-signal response has not yet been quantitatively investigated.

In this work, to study the high-speed response of surface-normal p-i-n detectors to short-pulsed optical inputs with small spot sizes, we made use of a dual-diode OCOG. This device was comprised of a p-i-n photodiode with a bulk intrinsic region on top of a reflective, multiple-quantum-well (MQW) p-i-n, electro-absorptive modulator diode. In this type of device, the voltage across the photodiode can be indirectly measured by shining onto the device a second beam of “probe” light that interacts only with the modulator diode. The voltage response of the photodiode to the original optical input, referred to as “control” input in Fig. 1, may be determined by simply recording the reflected probe light using a pump-probe technique. One advantage of this optical probing technique is that it avoids parasitic loading effects.

Below, we first present the response to increasing control pulse energies of a surface-normal p-i-n photodetector embodied in a dual-diode OCOG device. This is followed by a description of the simulations used to model the device dynamics and a comparison between the simulations and the data. Finally, we present data demonstrating only a relatively weak dependence of a photodetector’s recovery time to the spot size of incident light and discuss the implications.

Manuscript received June 23, 2003; revised November 3, 2003.

The authors are with the Ginzton Laboratory, Stanford University, Stanford, CA 94305 USA.

Digital Object Identifier 10.1109/JQE.2003.821533

II. LARGE-SIGNAL RESPONSE

The schematic of the dual-diode structure that we designed, fabricated, and tested is shown in Fig. 1. In operation of this structure, separate contacts are made to all three doped regions, the top n layer, the middle p layer and the lower n layer. Each of the two p-i-n diodes is separately reverse biased by individual voltage supplies. When a control pulse hits the upper reverse-biased photodiode, it photogenerates carriers that “vertically” separate (along the z axis) in the intrinsic region. As a result, the voltage across the photodiode is shielded in the vicinity of the control pulse.

In this type of device, the top and bottom n-layers are designed, ideally, to be highly conductive so that the overall voltage across the entire device at each “lateral” point (on the x - y plane) is held nearly constant. Consequently, the voltage change due to the carrier separation in the top diode is mimicked by an identical opposite voltage change in the reverse-biased bottom diode. Both diodes have their reverse bias voltages reduced locally by equal amounts. Note that it is the local voltage within the region near the optical spot that changes significantly. The resulting voltage dynamics are governed by predominantly local relaxation of these voltage changes through the finite conductivity of, primarily, the p-layer. These high-speed dynamics are not significantly influenced by the external circuit dynamics of the bias supplies. This, in turn, reduces the absorption of MQWs in the modulator diode for wavelengths near the heavy-hole exciton absorption peak as it blue-shifts with diminishing electric fields due to the quantum confined Stark effect. [18] The wavelength of the probe is chosen such that: 1) the probe is fully transmitted through the top photodiode and 2) the probe is initially substantially absorbed in the modulator diode by externally applying a proper bias. When that bias is internally reduced due to the voltage change across the photodiode, the absorption of the probe is reduced (its reflection is increased). Afterwards, this optically induced voltage shielding quickly relaxes through diffusive conduction, restoring the probe reflectivity near its initial level. Therefore, measuring the reflected power of the probe pulse provides an indirect measurement of the voltage across the top p-i-n photodiode. More in-depth descriptions of the behavior of these types of OCOG devices may be found in [15].

The OCOG device we used was an n-i-p-i(MQW)-n structure atop a distributed Bragg reflector (DBR) mirror. Details of the MBE-grown OCOG device are as follows. A DBR mirror centered at 855 nm at room temperature composed of 25 periods of alternating $\text{Al}_{0.08}\text{Ga}_{0.92}\text{As}$ and AlAs was grown on top of an n-doped GaAs substrate. This was followed by a short “cleaning” superlattice (30 periods of alternating GaAs and AlAs layers, each 20 Å thick). This provided a smooth surface following the DBR growth. The bottom-most $\text{Al}_{0.08}\text{Ga}_{0.92}\text{As}$ n layer was 5000 Å thick and doped at about 10^{18} atoms/cm³, followed by 69 MQWs with 50-Å AlAs barriers and 95-Å GaAs wells. On top of this, a 1.2- μm 10^{18} cm⁻³ p, 0.3- μm i, and 500-Å 10^{18} cm⁻³ n region of $\text{Al}_{0.08}\text{Ga}_{0.92}\text{As}$ were successively grown (including a final n-doped 50-Å GaAs cap layer). On the very top, an antireflection Si_3N_4 layer was sputtered. The resulting resistances per square of the top (n),

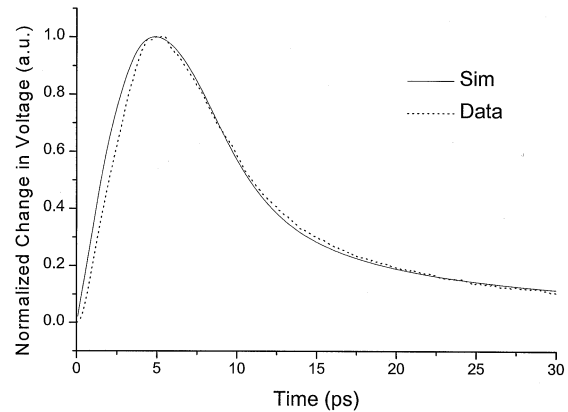


Fig. 2. Small-signal OCOG device behavior (0.66 pJ in a 5- μm radius spot) and simulation. The close fit between the simulation and data is strong support for a simulation model based on diffusive conduction and induced voltage change across the bottom diode.

middle (p), and bottom (n) doped layers were, respectively, 300 Ω/\square , 300 Ω/\square , and 10 Ω/\square . The similar magnitudes of the top and middle layers reduced the effectiveness of device operation but were accurately accounted for in the simulations, which modeled finite resistances in each layer. In this device, nonetheless, the time constant for the overall voltage dynamics was approximately twelve times shorter than that of the voltage relaxation across the top p-i-n photodetector itself, in part due to significant differences in capacitance per unit area. Thus, the overall voltage across the entire dual-diode stack recovered much more quickly than the voltage across the photodetector alone, and hence the overall voltage was kept relatively constant.

The temporal photodiode response to a control pulse was extracted by a pump-probe technique. In this procedure, the arrival of the sampling probe pulses on the device are delayed with respect to the arrival of the control pulse. A tunable short-pulse laser (SpectraPhysics Tsunami) was used to provide ~ 80 fs pulses at 855 nm for the probe pulse while the photodiode’s control pulse was frequency-doubled to 427 nm using a BBO crystal. These particular wavelength choices allowed the control input beam to be fully absorbed in the top photodiode and the probe beam to experience the voltage-sensitive absorption of the bottom modulator diode but not to be absorbed in the top photodiode. The measured reflectivity was approximately linearly proportional to the local voltage across the photodiode for the wavelengths and biases used in the tests of this OCOG device.

The small-signal response is presented in Fig. 2. Simulations based on diffusive conduction match the data well, supporting the premises that: 1) the spatially-localized voltage changes across the top photodiode induce voltage changes across the bottom modulator diode and 2) the photodiode’s local voltage relaxation response is due to diffusive conduction.

The response of the photodiode device to larger control pulse inputs is shown in Fig. 3, here presented by the measured reflectivity. At low energy densities (e.g., 0.66 pJ in a 5- μm radius spot), as the pulse energy rises, the magnitude of the voltage change across the diode increases in a correspondingly linear fashion. As the pulse energy continues to increase, however, the

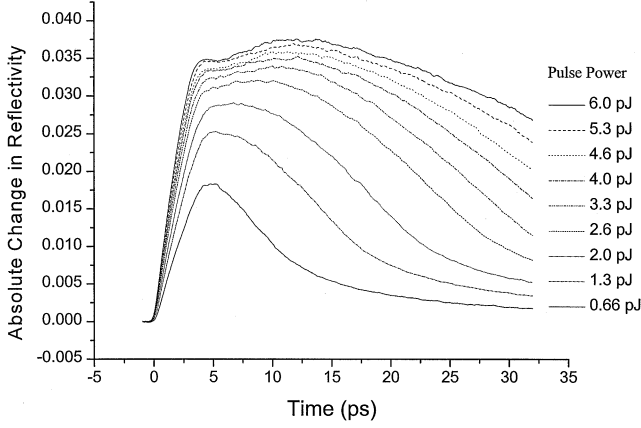


Fig. 3. OCOG response to large control inputs. Device tested with probe pulse power of $12 \mu\text{W}$, a $5\text{-}\mu\text{m}$ spot size radius, and -5 and -15-V bias across the top and bottom diode, respectively.

p-i-n photodetector response begins to deviate from the small-signal diffusive conduction-based decay. The magnitude of the change in voltage increases at a slower and slower rate with respect to increasing power, flattening out at the peak, and decays more slowly. At even higher energies (e.g., $\sim 5.0 \text{ pJ}$), the magnitude of the change in voltage clearly reaches a limit. Voltage decay is quite slow and has a completely different functional form than small-signal diffusive conduction.

III. THEORETICAL MODEL

In this section, we begin by presenting the general equations governing the device behavior. This is followed by descriptions of the assumptions and simplifications we made to allow simpler and faster calculations. The resulting model helps to explain the observed large-signal behavior of the device.

Carrier dynamics may be described by a combination of Poisson's and the continuity equations. Poisson's equation is given by

$$\nabla \cdot \mathbf{E} = \left(\frac{-q}{\epsilon} \right) (n - p + N_a - N_d) \quad (1)$$

where n , p , N_a , and N_d are, respectively, the free electron, free hole, fixed negative charge, and fixed positive charge densities where each is a function of position vector and time. The continuity equations are

$$\frac{\partial n}{\partial t} = G - R + \nabla \cdot \mathbf{j}_n, \quad \frac{\partial p}{\partial t} = G - R + \nabla \cdot \mathbf{j}_p \quad (2)$$

in which G is the carrier pair generation rate, and R is the carrier pair recombination rate. Here \mathbf{j}_n and \mathbf{j}_p are the electron and hole current densities, respectively, given by

$$\mathbf{j}_n = q\mu_n n \mathbf{E} + qD_n \nabla n \quad \mathbf{j}_p = q\mu_p p \mathbf{E} + qD_p \nabla p \quad (3)$$

where μ and D are the appropriate mobility and carrier diffusion coefficients either for electrons or holes.

As has been described elsewhere (e.g., [12]), in devices such as p-i-n diodes these equations may be used in part to show that any local voltage shielding that builds up due to vertical photo-generated carrier separation smoothes itself out laterally across

the device face as a result of diffusive conduction as expressed by

$$\frac{dV}{dt} = D_{\text{diffusion}}^{\text{voltage}} \nabla_{x,y}^2 V \quad (4)$$

where V is the voltage due to shielding across the intrinsic region and

$$D_{\text{diffusion}}^{\text{voltage}} = \frac{1}{R_{\text{sq}} C_{\text{area}}} \quad (5)$$

where R_{sq} is the sum of the resistance per square of the p- and n-layers and C_{area} is the capacitance per unit area determined by the thickness of the intrinsic layer. This behavior may be equivalently described as the effective lateral motion of the free carriers in the doped layers. [19]

When the incident spot of light is small compared to the area of the device face and $R_{\text{sq}} C_{\text{area}}$ is engineered to be of the order of a picosecond, voltage relaxation occurs on a picosecond time scale and is essentially independent of the RC time constant of the external circuitry.¹ If such an instantaneous surface-normal light pulse is spatially Gaussian, $V(r, t = 0)$ is then given by [16]

$$V(r, t = 0) = V_M \exp\left(\frac{-r^2}{\frac{w_0^2}{2}}\right) \quad (6)$$

where

$$V_M \equiv \frac{Q_{\text{TOT}}}{C_A \pi \left(\frac{w_0}{\sqrt{2}}\right)^2}. \quad (7)$$

Here Q_{TOT} is the total photogenerated charge and w_0 is the radius of the control spot. r is the lateral radial distance from spot center. The spatio-temporal impulse response of built-up voltage is the analytic solution to (4) given by

$$V_{\text{response}}^{\text{impulse}}(r, t) = V_M \left(\frac{\tau}{t + \tau} \right) \exp\left(\frac{-r^2}{4D(t + \tau)}\right) \quad (8)$$

with

$$\tau \equiv \left(\frac{w_0}{\sqrt{2}}\right)^2 \frac{1}{4D_{\text{diffusion}}^{\text{voltage}}}. \quad (9)$$

The effective *lateral* carrier motion in the doped layers due to voltage diffusion is thus several orders of magnitude faster than the lateral motion of carriers in the intrinsic region, this latter diffusion being primarily due to regular (ambipolar) carrier diffusion, i.e., $D_{\text{diffusion}}^{\text{voltage}} \gg D_{\text{ambipolar}}$. Note that (8) describes both the on- and off-center responses for a single-layer, p-i-n device. The functional form in the multilayer OCOG device we tested is slightly different due to the coupling between the layers (see Appendix A), although the response was qualitatively the same as for the single-layer case.

¹The overall voltage that builds up across the entire device face does indeed relax through the external circuitry. For single-pulse behavior, this response may be ignored; when modeling many consecutive pulses or extended periods of time, this external relaxation should also be included, though it effectively corresponds only to a slight overall average change in device bias voltage if the external response is relatively slow compared to voltage diffusion.

On the other hand, *vertical* motion of the carriers is due to drift and regular diffusion. Even though the regular carrier diffusion coefficient may be orders of magnitude smaller than the voltage diffusion coefficient, for large-signal response, regular carrier diffusion along the z axis should *not* be ignored, including diffusion within the doped layers. Although such diffusion effects are small when the carriers are moving at saturated drift velocities, large pulse intensities result in strong shielding that can significantly reduce the drift component of vertical motion. As a result, the vertical carrier diffusion becomes an important factor in carrier dynamics.

In many photodiodes and other devices, the thickness of the intrinsic layer is less than or equal to one or two micrometers while the spot size of the incident light is often several microns or more in diameter. Consequently, the relative time for photo-generated carriers of a pulse of light to separate vertically to the doped layers (roughly, tens of picoseconds or less) is also much smaller than any significant lateral regular diffusion of the carriers in the intrinsic region. A simplifying assumption may therefore be made that lateral regular carrier diffusion inside the intrinsic region may be disregarded. Taking these ideas together, the device response can be modeled by restricting carrier motion to arise only from vertical carrier drift along the z axis across the intrinsic region and lateral voltage diffusion across the cross-sectional plane of the doped regions.

To simplify the calculations (particularly those related to diffusive conduction), only the voltage at the center of the incident spot was explicitly determined.

A few other assumptions are also made.

- 1) The incident control and probe pulses have a Gaussian spot intensity distribution and are small compared to the lateral dimensions of the photodiode.
- 2) Drift-diffusion equations are valid (e.g., we may ignore ballistic effects, temperature gradients, etc.).
- 3) Recombination may be ignored (recombination times are typically on the order of nanoseconds while the response time of the devices considered here was 100 ps or less).
- 4) The diffusion coefficient is independent of the electric field and carrier density.
- 5) The capacitance per unit area between the doped layers is constant, independent of the presence of photogenerated carriers.

Carrier motion within the photodiode can thus be described using just the following few equations. In the intrinsic region (where carrier motion is vertical), (1) becomes

$$E(z, t) = E_{\text{built-in}} + E_{\text{applied}} + \left(\frac{-q}{\varepsilon}\right) \int_{\text{top}}^{\text{bottom}} (n(z, t) - p(z, t)) dz. \quad (10)$$

In the integral above, bottom and top refer to the bottom and top of the upper p-i-n photodiode. The steady-state carrier densities are accounted for in the built-in and applied electric fields;

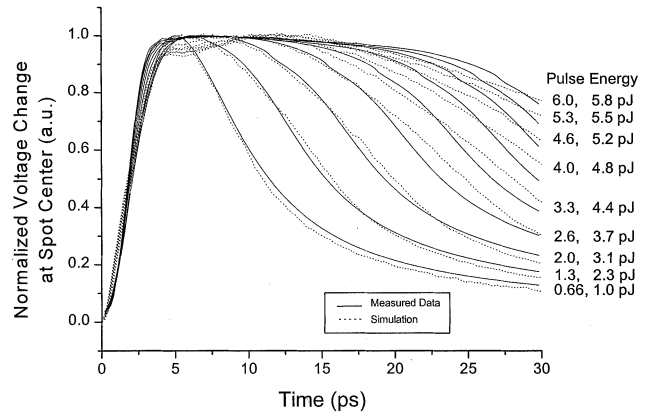


Fig. 4. Measured (dotted lines) and simulated (solid lines) normalized changes in voltage as a function of time for various control pulse powers for a spot size radius of $5 \mu\text{m}$ with -5-V and -15-V reverse bias applied across the top and bottom diodes, respectively. Values of the actual (left column) and simulated (right column) incident power are presented in the figure's legend. Simulation parameters included resistances per square of $300 \Omega/\square$, $300 \Omega/\square$, and $10 \Omega/\square$ for the top n, p, and bottom n layers with top and bottom diode capacitances per unit area of 0.3 and $0.1 \text{ fF}/\mu\text{m}^2$.

hereafter n and p are now the deviations from steady-state carrier densities. Equations (2) and (3) simplify to

$$\frac{\partial n(z, t)}{\partial t} = G + \nabla_z j_n(z, t) \quad (11)$$

$$\frac{\partial p(z, t)}{\partial t} = G + \nabla_z j_p(z, t) \quad (12)$$

$$j_n(z, t) = q\mu_n n(z, t) E(z, t) + qD_n \nabla_z n(z, t)$$

$$j_p(z, t) = q\mu_p p(z, t) E(z, t) + qD_p \nabla_z p(z, t) \quad (12)$$

whereas in the doped layers (where carrier motion is principally lateral)

$$V(r=0, t) = \int_0^t \left(V_m(t') V_{\text{impulse response}}(r=0, t-t') \right) dt' \quad (13)$$

where $V(r=0, t)$ is the overall voltage shielding at spot center and $V_{\text{impulse response}}$ is the voltage diffusion impulse response function for the p-i-n photodetector portion of the device. Because of these simplifications, the simulation calculation time (on the order of a minute) is short compared to a complete coupled three-dimensional (3-D) model.

A time-iterative model was used to simulate the dynamic behavior of the device based on the theory developed in this section; the details of the simulation procedure are provided in Appendix B.

IV. SIMULATION RESULTS AND DISCUSSION

The fit between the large-signal data and simulation in Fig. 4 provides support for the following hypothesis describing the local large-signal response in photodetectors. When large control energies are used, the magnitude of the overall reverse bias (applied bias plus the "built-in" voltage) becomes a critical factor. If there are enough photogenerated electrons and holes, the shielding electric field that they create as they vertically separate rapidly reduces the local electric field between them to near zero. As a result, carriers in that low-field region between them slow down and may stop drifting.

Carriers at the edge of the shielded region still see a largely unshielded field and continue to drift vertically. As they move, the shielded space expands in their wake. The result is still a rapid “turn-on” but followed by a much slower decay as many of the carriers become trapped in low-field regions of the intrinsic layer. Two ongoing processes help alleviate this situation. One is regular carrier diffusion in the vertical z direction. The other process is lateral diffusive conduction. Diffusive conduction constantly eats away at the screening voltage. As it does so, the electric field in the intrinsic region grows back, allowing carriers to continue to drift. As the carriers move, however, they once again shield the field and the process repeats itself. The carriers move slowly but, eventually, they are completely extracted from the intrinsic region. After that point any remaining voltage build-up decays away, limited only by diffusive conduction.

The above description and explanation make physical sense and the simulations exhibit qualitative behavior similar to the device response. However, when the intensity is particularly large, the simulations do not match the data as well, recovering too quickly at longer times. The most likely reason these effects occur in the simulations is due to the simplification of only simulating the response of the device at the center of the incident light. The reflected light signal, of course, is affected by the voltage distribution over the entire beam size. The off-center $r \neq 0$ response of diffusive conduction is distinct and follows a form similar to that of (8). How off-center behavior becomes important with large signals is addressed below.

With large incident light intensities, the voltage change across the photodiode in the center quickly “saturates” (the device is fully shielded). The voltage shielding at off-center points, however, continues to rise until the voltages there saturate, too. Due to this nonlinearity, the initial Gaussian shape of the voltage gradient distorts, flattening out with increasing intensities for large signals. This reduces the voltage diffusion speed. Additionally, the probe pulse has a finite spot size (equal to the spot size of the pump pulse), and so it samples on-center as well as off-center points. As expressed in (8), the response of off-center voltage decay slows with increasing radial distance. Taken together, when pump intensities are high, the resulting reflectivity measurement shows a slower decay due to its off-center behavior than do the simulations. Modeling these effects would require full 3-D analysis instead of the simplified two one-dimensional (1-D) equations used here.

As the incident power increases, the time needed for the change in reflectivity to crest grows (and a “dip” in reflectivity also develops at short times). This, too, is likely due to the sampling of off-center points by the probe beam. As the distance from the spot center increases, the initial rise-time of the voltage shielding lengthens; it takes time for the initial shielding voltage to diffuse, increasing the shielding at distant points. Thus, off-center points take longer to reach their maximum voltage change and, because the probe beam samples them as well, the overall change in reflectivity seems to peak at a later time.

V. FIELD BLEACHING CASE STUDY

Surface-normal photodiodes are commonly illuminated with spot sizes smaller than the diode mesas to prevent the

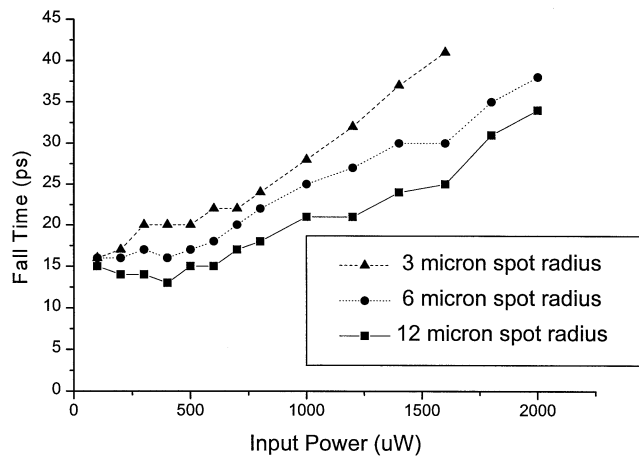


Fig. 5. Photodetector response to incident optical short pulses with various input power for different spot sizes. Response time (the $1/e$ fall time) of the photodetector increases with increasing incident power due to field-bleaching and related effects. Note, however, that the response time is only a relatively slow function of incident spot size for the same total energy. The power needed to double the response time with a large spot ($12\text{-}\mu\text{m}$ radius almost completely fills the photodetector), is $\sim 1800\ \mu\text{W}$. For a $3\text{-}\mu\text{m}$ spot radius, 16 times more intense, the power needed to slow the response time down so that it doubles is not $1800/16 \sim 115\ \mu\text{W}$, but actually $\sim 1100\ \mu\text{W}$, greater than 50% of the power needed for the $12\text{-}\mu\text{m}$ spot.

optical power loss and slow diffusion tail that occur when the photodiodes are overfilled. It is therefore critical to understand p-i-n photodetector response to high-power, small-spot-size optical inputs, particularly because field bleaching due to photogenerated carrier separation can significantly degrade detector response.

It is possible, however, to dramatically limit the field bleaching by taking advantage of the distributed RC nature of the photodetector. As the spot size shrinks, “saturation” occurs at a lower energy level. However, this energy level is significantly larger than might otherwise be expected. This is because the voltage shielding that builds up due to carrier separation is also constantly being laterally diffused across the rest of the device, even as the carriers are separating, at a rate that *increases* with diminishing spot size. Moreover, this effect may be enhanced with proper design because lower internal resistance-per-square also provides faster voltage relaxation, yielding faster response and higher saturation power. Lowering the capacitance is more difficult than simply increasing the intrinsic layer thickness because doing so slows the vertical transit time in the photodetector and also increases the bias voltage needed. However, modifications that can reduce the dielectric coefficient of the intrinsic region may be helpful. Generally speaking, it is much easier to instead adjust the resistance. For example, use of transparent conducting material such as indium tin oxide (ITO) may be used to lower the resistance per square of the top doped layer while still maintaining high transmission and low absorption compared to, say, doped semiconductor or thin metallic layers.

This surprising behavior is demonstrated in Fig. 5, showing response time (the time taken for the photocurrent to drop $1/e$) as a function of energy for different spot sizes. In this experiment, we used a $25\text{-}\mu\text{m}$ -diameter New Focus 25-GHz photodetector. Its $0.8\text{-}\mu\text{m}$ -thick and highly n-doped (8×10^{18}) InAlAs bottom

layer and 100-Å gold top cover layer provided low resistance per square, and its capacitance per unit area was 0.1 fF/ μm^2 , providing a fast diffusive conduction response. Two-picosecond control pulses at 850 nm with an 82-MHz repetition rate were used as the incident light, and a Hewlett Packard 20-GHz oscilloscope was used to measure the dynamic response of the photodetector. Spot-size measurements were made by imaging the beam spots on the photodetector onto a CCD camera and using a standard oscilloscope to view the resulting video output to determine the $1/e^2$ widths of the spots.

As expected, for a given spot size, at low energies the response is flat since little bleaching occurs; at larger energies field bleaching slows down device recovery. If field bleaching was due solely to the incident intensity but otherwise unaffected by spot size then, to first order, one would expect that by halving the spot size radius, and thus quadrupling the intensity, the incident energy that is needed to double the response time from its low-intensity value of ~ 15 ps would drop by 1/4. Using this logic, reducing the spot size radius from 12 to 3 μm should result in a ~ 30 ps response time at 1/16 the incident energy. This does not happen, as the data demonstrates clearly. Instead, we see that there is only a relatively weak dependence of the incident energy needed for response time doubling on spot size reduction (reducing the radius by 1/4 results in approximately only halving the incident energy that is needed to double the response time). This dependence may be due to a variety of higher order effects, including photodetector boundary edge-effects and the nonlinear responses described previously in this paper. One disadvantage of shrinking the spot size is that the higher intensity will lead to greater localized Joule heating, which may enhance the potential for thermal runaway due to increased dark current [12], [20].

Thus, with a small distributed RC decay, it is possible to make the input power at which field bleaching occurs become almost independent of spot size, enabling the use of small spots in a properly designed photodetector. The underlying reason for this independence on spot size can be traced back to (9), which shows that the diffusive conduction time constant is proportional to the spot area (i.e., $\propto \omega_0^2$)

VI. CONCLUSION

To understand better photodetector behavior, we used a dual-diode device combined with a pump-probe technique to study local voltage dynamics. The response of p-i-n photodetectors depends on numerous factors including, if the spot size is small, local voltage diffusion. If the incident power is sufficient to shield the reverse bias significantly, device recovery slows due primarily to the reduction of the vertical drift current. Device recovery is enhanced due to voltage diffusion. Inclusion of regular carrier diffusion along the z axis and injection of carriers from the doped regions is essential for device modeling. Accounting for off-center carrier motion would improve the simulation method described here, although at the cost of significantly increased simulation time. Ultimately, device response becomes limited by inductive effects (not modeled in the simulation) as diffusive conduction becomes electromagnetic propagation and radiation.

For high-speed response, p-i-n diodes are typically made very small primarily to reduce their capacitance. In doing so, their response becomes strongly dependent on the external circuitry and the corresponding load. As shown here, however, the use of small incident spots on larger devices can provide a fast (optically probed) response. In essence, the incident spot only discharges the local capacitance of the spot and is able to quickly recover by spreading the voltage over the rest of the device—for the most part independently of the external circuitry. This might be useful, for example, in high-speed gated photodetection applications. Moreover, as the spot size shrinks, the required optical power diminishes and the device response improves. Simulations also show that small spot sizes cause negligible additional field screening for properly designed photodetectors for a given input power.

APPENDIX A MULTILAYER DIFFUSIVE CONDUCTION

The general expression for the impulse response functions for the dual-diode OCOG device used for large-signal tests and simulation is presented here. For derivation details, see [1]. In the expression below, layers A , B , and C , are the top n, middle p, and bottom n regions of the device. V_{AB} is the voltage shielding between layers A and B , while V_{CB} is the induced voltage shielding between layers C and B . The coupled, two-layer voltage diffusion at spot center is given by

$$\begin{pmatrix} V_{AB}(r=0, t) \\ V_{CB}(r=0, t) \end{pmatrix} = \begin{pmatrix} \frac{V_0}{(1 - \frac{D_A - \lambda_+}{D_A - \lambda_-})} \frac{\tau_+}{t + \tau_+} - \frac{V_0}{(\frac{D_A - \lambda_-}{D_A - \lambda_+} - 1)} \frac{\tau_-}{t + \tau_-} \\ \frac{V_0}{D_A \phi_A} \frac{1}{(\frac{1}{D_A - \lambda_+} - \frac{1}{D_A - \lambda_-})} \left[\frac{\tau_+}{t + \tau_+} - \frac{\tau_-}{t + \tau_-} \right] \end{pmatrix} \quad (\text{A1})$$

where

$$\lambda_{\pm} = \frac{D_{22} + D_{11} \pm \sqrt{(D_{22} + D_{11})^2 - 4(D_{22}D_{11} - D_{12}D_{21})}}{2} \quad (\text{A2})$$

$$\tau_{\pm} = \left(\frac{w_0}{\sqrt{2}} \right)^2 \frac{1}{4\lambda_{\pm}} \quad (\text{A3})$$

and

$$\begin{aligned} \tilde{D} &= \begin{pmatrix} D_{11} & D_{12} \\ D_{21} & D_{22} \end{pmatrix} \\ &= \begin{pmatrix} \frac{1}{C_{AB}} \frac{1}{(R_A + R_C \phi_C)} & \frac{-1}{C_{AB}} \frac{\phi_C}{(R_A + R_C \phi_C)} \\ \frac{-1}{C_{CB}} \frac{\phi_A}{(R_C + R_A \phi_A)} & \frac{1}{C_{CB}} \frac{1}{(R_C + R_A \phi_A)} \end{pmatrix} \end{aligned} \quad (\text{A4})$$

in which

$$\phi_A \equiv \frac{R_B}{R_B + R_A} \quad \phi_C \equiv \frac{R_B}{R_B + R_C} \quad (\text{A5})$$

$$D_A \equiv \frac{1}{C_{AB}} \frac{1}{(R_A + R_C \phi_C)} \quad D_C \equiv \frac{1}{C_{CB}} \frac{1}{(R_C + R_A \phi_A)}. \quad (\text{A6})$$

In the above expressions, R_i is the resistance per square of the i^{th} doped layer, and C_{ij} is the capacitance per area of the intrinsic region between doped layers i and j .

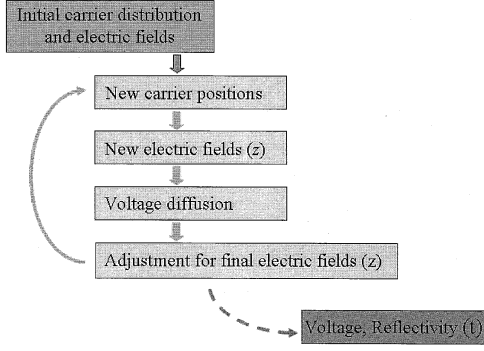


Fig. 6. Schematic flowchart of time-iterative large-signal computer simulation.

APPENDIX B SIMULATION DETAILS

A time-iterative model was used to simulate the dynamic behavior of the device, as shown schematically in Fig. 6. After determining the generating function of the photogenerated carriers and electric fields, the primary loop of the simulation was initiated. The internal structure of the simulation consisted of three sections:

- determining the new carrier distribution as a function of vertical (z) position; newly generated carriers were included in this step;
- determining the electric field as a function of z ;
- determining the electric field as a function of z ;

Each of these sections is described in detail below.

A. Generating Function

The time and spatial dependence of the generating function G of (11) was based on the particular experimental setup we used. The absorption length of the incident 427-nm light in $\text{Al}_{0.08}\text{Ga}_{0.92}\text{As}$ is short, about 33 nm. [21] The control input, as a consequence, was absorbed primarily in the top n-doped layer and the top of the intrinsic layer beneath it.² Given the duration of the control pulse, at each time step the number of new photogenerated carriers as a function of vertical position in these top two layers may be calculated.

It was important to account for the injection of photogenerated carriers from the thin (50 nm), top n-doped layer into the intrinsic region. In our simulations this was modeled by assuming that injection was due to thermionic emission, [22] We can thus write the impulse response of an instantaneous pulse that creates n_{photogen}^0 carriers

$$\frac{dn}{dt} = n_{\text{photogen}}^0 v_{\text{th}} \exp(-v_{\text{th}} t) \quad (\text{B1})$$

where v_{th} is the thermal velocity, here set equal to 0.6×10^6 cm/s. We use (B1) to determine how many photogenerated carriers initially enter the intrinsic region in the

²It is worth mentioning that the very short absorption length of the pump pulse (due to the short wavelength we used) affects the p-i-n response. If instead, for example, the absorption length were significantly longer so that carrier absorption was approximately evenly distributed across the intrinsic region, the initial voltage shielding (turn-on) time would shrink with increasing incident power. As the device was tested here, the turn-on time is nearly independent of magnitude of the control power.

first “bin” near the n-layer. From this point, the carriers become subject to drift and diffusion, (12), as described in the section below. The electrons tend to quickly move back into the doped n layer while the holes cross the entire intrinsic region.

B. Carrier Distribution

The carriers in the doped layers were determined first. Carrier density in these regions built up as the photogenerated carriers were pulled out of the intrinsic region but decayed as the carrier density at the spot center was laterally dispersed due to voltage diffusion. The number present at the beginning of each time step was determined by the difference between the overall voltage across the device less the voltage due to the space charge of carriers still in the intrinsic region. The carrier number equaled the resulting potential divided by the capacitance of the intrinsic region. Vertical diffusion within the doped regions was also accounted for.

In the intrinsic region, carriers drifted due to the vertical electric field present at their position and vertically diffused due to the local carrier gradient. The drift velocity’s field dependence for both carrier types was modeled based on references [23] and [24] as follows:

$$v_{\text{hole}}(E) = v_{\text{hole}}^{\text{sat}} \left(1 - \exp\left(-\frac{E}{E_{\text{hole}}^{\text{sat}}}\right) \right) \quad (\text{B2})$$

$$v_{\text{elec}}(E) = \frac{\mu_e E + v_{\text{elec}}^{\text{sat}} \left(\frac{E}{E_{\text{elec}}^{\text{peak}}} \right)^4}{1 + \left(\frac{E}{E_{\text{elec}}^{\text{peak}}} \right)^4} \quad (\text{B3})$$

using $v_{\text{hole}}^{\text{sat}} = 0.7 \times 10^7$ cm/s, $E_{\text{hole}}^{\text{sat}} = 2 \times 10^4$ V/cm, $v_{\text{elec}}^{\text{sat}} = 1.1 \times 10^7$ cm/s, and $E_{\text{elec}}^{\text{peak}} = 4 \times 10^5$ V/cm.

To determine the new positions of the carriers, a finite difference method approach was used to solve the vertical drift-diffusion equations for the electrons and holes based on the Crank–Nicholson method. To help numerical stability of the simulation, a 50–50 average between explicit and implicit forward time-centered space (FTCM) functions [25] was used with 10-fs time steps and 10-nm vertical spatial steps.³

C. Electric Field (z)

Once the vertical motion of the carriers had been determined, the electric field as a function of z in the intrinsic region was calculated, accounting for both the applied and built-in fields as well as the fields due to space charge effects. The thickness of the intrinsic region typically is significantly smaller than the spot size width. Consequently, the field may be assumed to vertical everywhere. This is what allows the use of the integral on the right-hand side of (10) to be over z only, significantly simplifying Poisson’s equation.

At each vertical location, summing the electric fields from the charge densities along the z axis provides the field due to the space charge in the device at spot center. When combined

³The stability condition of the finite difference method is given by $(|v| \Delta t / \Delta z) \leq 1$ [25]. For the parameters and step size we used, to avoid instability, electron vertical diffusion coefficients with values less than $50 \text{ cm}^2/\text{s}$ were required. The electron diffusion coefficient is approximately $175 \text{ cm}^2/\text{s}$, however. To ensure stability, a value of only $40 \text{ cm}^2/\text{s}$ was therefore used.

with the built-in and applied fields, this process provides a good approximation to the solution to Poisson's equation.

D. Voltage Changes due to Voltage Diffusion

At this point, vertical motion and field calculations have been accounted for. The lateral voltage decay (and thus lateral carrier motion), however, has not. To do so, at each time period the overall change in voltage at spot center due to vertical carrier motion at each time period is recorded. The impulse response of the top n-i-p layers was coupled with the behavior of the lower p-i (MQW)-n layers, precluding the use of (8) for a simple p-i-n device.⁴ The top and bottom layers' diffusive conduction behaviors were calculated by solving the coupled multilayer diffusion equations as outlined in [1] (for the solution used, see the Appendix).⁵

E. Overall $V(t)$

The remaining voltage change from a particular previous time step is obtained by multiplying its original magnitude with the diffusive conduction impulse response. This impulse response is a function of the time difference that has elapsed between that specific time step and the current moment. Thus, the overall voltage at a particular time period can be calculated by summing the remaining voltage change of each previous time step and adding it to the constant built-in and applied biases [a discrete form of (13)].

The voltage behavior of the device was determined by measuring the voltage-sensitive reflectivity of the probe pulse. To match this, the simulation determined what the reflectivity of the probe pulse should be by: 1) determining the voltage across the bottom diode as a function of time due to the top diode's voltage⁶ and 2) using the measured empirical relation between the reflectivity and the voltage applied across the modulator diode.

REFERENCES

- [1] M. B. Yairi, H. V. Demir, and D. A. B. Miller, "Optically controlled optical gate with an optoelectronic dual diode structure – theory and experiment," *Opt. Quantum Electron.*, vol. 33, pp. 1035–1054, 2001.
- [2] M. B. Yairi, C. W. Coldren, D. A. B. Miller, and J. S. Harris Jr., "High-speed, optically-controlled surface normal optical switch based on diffusive conduction," *Appl. Phys. Lett.*, vol. 75, pp. 597–599, 1999.
- [3] M. Dentan and B. de Cremoux, "Numerical simulation of the nonlinear response of a p-i-n photodiode under high illumination," *J. Lightwave Technol.*, vol. 8, pp. 1137–1144, 1990.
- [4] K. J. Williams, R. D. Esman, and M. Dagenais, "Effects of high space-charge fields on the response of microwave photodetectors," *IEEE Photon. Technol. Lett.*, vol. 6, pp. 639–641, 1994.
- [5] J. Harari, G. H. Jin, F. Jourmet, J. Vandecasteele, J. P. Vilcot, C. Dalle, M. R. Friscourt, and D. Decoster, "Modeling of microwave top illuminated PIN photodetector under very high optical power," *IEEE Trans. Microwave Theory Tech.*, vol. 44, pp. 1484–1487, 1996.
- [6] Y. Zebda and S. Abu-Helweh, "Bandwidth improvement of a homo-junction p-i-n photodiode," *IEEE J. Quantum Electron.*, vol. 33, pp. 1333–1337, 1998.
- [7] Y.-L. Huang and C.-K. Sun, "Nonlinear saturation behaviors of high-speed p-i-n photodetectors," *J. Lightwave Technol.*, vol. 18, pp. 203–212, 2000.
- [8] K. J. Williams and R. D. Esman, "Nonlinearities in p-i-n microwave photodetectors," *J. Lightwave Technol.*, vol. 14, pp. 84–96, 1996.
- [9] S. Noor Mohammad and S. T. H. Abidi, "Theory of saturation photocurrent and photovoltage in p-n junction solar cells," *J. Appl. Phys.*, vol. 61, pp. 4909–4919, 1987.
- [10] C.-K. Sun, I.-H. Tan, and J. E. Bowers, "Ultrafast transport dynamics on p-i-n photodetectors under high-power illumination," *IEEE Photon. Technol. Lett.*, vol. 10, pp. 135–137, 1998.
- [11] J. S. Paslaski *et al.*, "High-power microwave photodiode for improving performance of rf fiber optic links," in *Proc. SPIE*, vol. 2844, 1996, pp. 110–119.
- [12] K. J. Williams and R. D. Esman, "Design considerations for high-current photodetectors," *J. Lightwave Technol.*, vol. 17, pp. 1443–1454, 1999.
- [13] P. J. Bradley, C. Rigo, and A. Stano, "Carrier induced transient electric fields in a p-i-n InP-InGaAs multiple-quantum-well modulator," *IEEE J. Quantum Electron.*, vol. 32, pp. 43–52, 1996.
- [14] C. M. Yang, E. Canoglu, E. Garmire, K. W. Goossen, J. E. Cunningham, and W. Y. Jan, "Measurement of effective drift velocities of electrons and holes in shallow multiple-quantum-well p-i-n modulators," *IEEE J. Quantum Electron.*, vol. 33, pp. 1498–1506, 1997.
- [15] H. Wang, F. J. Effenberger, P. LiKamWa, and A. Miller, "Ultrafast cross-well carrier transport in a strained multiple-quantum-well InGaAs-GaAs p-i-n modulator," *IEEE J. Quantum Electron.*, vol. 33, pp. 192–197, 1997.
- [16] J. A. Cavaillès, D. A. B. Miller, J. E. Cunningham, P. LiKamWa, and A. Miller, "Simultaneous measurements of electron and hole sweep-out from quantum wells and modeling of photoinduced field screening dynamics," *IEEE J. Quantum Electron.*, vol. 28, pp. 2486–2497, 1992.
- [17] D. Mahgerefteh, C.-M. Yang, L. Chen, K. Hu, W. Chen, E. Garmire, and A. Madhukar, "Picosecond time-resolved measurements on electroabsorption in an InGaAs/GaAs multiple quantum well p-i-n modulator," *Appl. Phys. Lett.*, vol. 61, pp. 2592–2594, 1992.
- [18] D. A. B. Miller, D. S. Chemla, T. C. Damen, A. C. Gossard, W. Wiegman, T. H. Wood, and C. A. Burrus, "Electric field dependence of optical absorption near the bandgap of quantum well structures," *Phys. Rev. B*, vol. 32, pp. 1043–1060, 1985.
- [19] M. B. Yairi and D. A. B. Miller, "Equivalence of diffusive conduction and giant ambipolar diffusion," *J. Appl. Phys.*, vol. 91, pp. 4374–4381, 2002.
- [20] A. Nespola *et al.*, "Failure analysis of travelling wave MSM distributed photodetectors," in *Proc. Int. Electron Device Meeting*, San Francisco, CA, 1998, pp. 669–672.
- [21] S. Adachi, *GaAs and Related Materials*, Singapore: World Scientific, 1994, p. 387.
- [22] S. M. Sze, *Physics of Semiconductor Devices*. New York: Wiley, 1981, pp. 255–256.
- [23] H. W. Thim, "Computer study of bulk devices with random one-dimensional doping fluctuations," *J. Appl. Phys.*, vol. 39, pp. 3897–3904, 1968.
- [24] D. M. Barry, C. M. Snowden, and M. J. Howes, "A numerical simulation of high speed GaAs photodetectors," in *Proc. Microwave Devices, Fundamentals and Applications, IEE Colloquium*, 1988, pp. 5/1–5/6.
- [25] W. H. Press, S. A. Teukolsky, W. T. Vetterling, and B. P. Flannery, *Numerical Recipes in C: The Art of Scientific Computing*. Cambridge, U.K.: Cambridge Univ. Press, 1992, p. 51, 838, 849.

⁴This coupling behavior is what is responsible for the induced voltage across the bottom diode. The response of the top diode does not differ significantly from its isolated behavior except that the voltage shielding buildup magnitude is reduced as if placed across a voltage divider.

⁵To determine the voltage across the device, it is assumed that there is no field across the doped regions themselves (in spite of local space charge effects).

⁶Calculation of the bottom diode's voltage behavior was straight forward. Because no carriers are generated there due to the control pulse, no carrier motion nor space-charge effects need be calculated. Instead, simply knowing the amount of added voltage shielding in the top p-i-n diode due to carrier separation ($V_m(t)$ in (13)) but using the impulse response function of voltage diffusion for the bottom diode provides all the necessary information.

Micah B. Yairi received the B.S. degree in engineering physics and the B.A. degree in economics from the University of Illinois at Urbana-Champaign in 1994, the M.Phil. degree in economics from the University of Cambridge, Cambridge, U.K., in 1995, and the M.S. and Ph.D. degrees in applied physics from Stanford University, Stanford, CA, in 1997 and 2001, respectively. His doctoral research focused on high-speed all-optical switching under the supervision of Prof. D. A. B. Miller.

While at the University of Cambridge, he was a Fulbright Scholar. He has joined Los Gatos Research, Mountain View, CA, as a Senior Physicist, where his work focuses on photonic microstructures and high-pressure, chip-based microfluidic projects.

Hilmi Volkan Demir received the B.Sc. degree in electrical and electronics engineering from Bilkent University, Ankara, Turkey, in 1998 and the M.S. degree from Stanford University, Stanford, CA, in 2000. He is currently working toward the Ph.D. degree under the supervision of Prof. D. A. B. Miller in the Department of Electrical Engineering at Stanford.

He is currently an Intel Research Assistant at Ginzton Laboratory, Stanford University. His research work focuses on the development of novel ultrafast photonic devices incorporating quantum-well structures for future optical networks.

Mr. Demir was a recipient of Bilkent Board of Trustees Scholarship for 1994–1998 and an Edward L. Ginzton Laboratory Rotation Fellowship for 1998–1999. He was an invited participant of London International Youth Science Forum, U.K., in 1994, a sponsored exchange student at Purdue University, IN, in 1997, a selected participant of National Union of Israeli Students' exchange program, Israel, in 1998, and one of the Stanford-Berkeley Innovator's Challenge Finalists in 2003.

Petar B. Atanackovic (M'00) was born in Adelaide, Australia, 1967. He received the B.Sc. (Hons) and Ph.D. degrees from the University of Adelaide, Adelaide, Australia. His Ph.D. work dealt with the growth and fabrication of novel II-VI quantum devices.

He was a Senior Research Scientist with the Defence Science and Technology Organization, Australia from 1997 to 2001, working on analog-to-digital conversion using photonic over-sampling techniques and novel optoelectronic III-V quantum devices. From 1999 to 2001, he was a Visiting Researcher at Ginzton Laboratories, Stanford University, CA. His work at Stanford dealt with the growth of novel GasAs- and InP-based quantum devices using molecular beam epitaxy. In 2001, he joined Translucent Photonics Inc., Palo Alto, CA, where he is currently exploring ultrahigh optoelectronic integration technologies.

David A. B. Miller (M'84–SM'89–F'95) received the B.Sc. degree from St. Andrews University, St. Andrews, U.K., and the Ph.D. degree from Heriot-Watt University, Edinburgh, U.K., in 1979.

He was with Bell Laboratories from 1981 to 1996 as a Department Head from 1987, latterly of the Advanced Photonics Research Department. He is currently the W. M. Keck Foundation Professor of Electrical Engineering at Stanford University, Stanford, CA, and Director of the Ginzton and Solid State and Photonics Laboratories, Stanford, CA. His research interests include quantum-well optoelectronic physics and devices, and fundamentals and applications of optics in information, sensing, switching, and processing. He has published more than 200 scientific papers and holds over 40 patents.

Dr. Miller has served as a Board member for both the Optical Society of America (OSA) and IEEE Lasers and Electro-Optics Society (LEOS) and in various other society and conference committees. He was President of IEEE LEOS in 1995. He was awarded the Adolph Lomb Medal and R. W. Wood Prize from the OSA, the International Prize in Optics from the International Commission for Optics, and an IEEE Third Millennium Medal. He is a Fellow of the Royal Society of London, OSA, and the American Physical Society and holds an honorary degree from the Vrije Universiteit Brussel.